Title: Subduction Zone Interface Structure within the Southern M_W9.2 1964 Great Alaska Earthquake Asperity: Constraints from Receiver Functions Across a Spatially Dense Node Array

Authors: Evans A. Onyango[1*], Lindsay L. Worthington[1], Brandon Schmandt[1], Geoffrey Abers[2]

***Corresponding Author:**

Evans A. Onyango, eaonyango@unm.edu

Department of Earth and Planetary Sciences, Northrop Hall, 221 Yale Blvd NE, University of New Mexico, Albuquerque, New Mexico 87131, USA.

Affiliations:

[1]Department of Earth and Planetary Sciences, Northrop Hall, 221 Yale Blvd NE, University of New Mexico, Albuquerque, New Mexico 87131, USA.

[2]Department of Earth and Atmospheric Sciences, Cornell University, 112 Hollister Drive, Ithaca, NY, 14853-1504, USA.

Key Points:

- We present receiver function imaging from a dense three-component nodal array deployment on Kodiak Island above the subducting Pacific Plate.
- A clear slab Moho conversion is found but, in contrast to the Kenai Peninsula, there is no evidence of a low-velocity layer atop the slab.
- The 1964 Great Alaska Earthquake ruptured across structural segments with heterogeneous plate interface properties.

Abstract

We conduct a high-resolution teleseismic receiver function investigation of the subducting plate interface within the Alaskan forearc beneath Kodiak Island using data collected as part of the Alaska Amphibious Community Seismic Experiment in 2019. The Kodiak node array consisted of 398 nodal geophones deployed at ~200 m spacing on northeastern Kodiak Island within the southern asperity of the 1964 Mw9.2 Great Alaska earthquake. Receiver function images at frequencies of 1.2 and 2.4 Hz show a coherent, slightly dipping velocity increase at ~30-40 km depth consistent with the expected slab Moho. In contrast to studies within the northern asperity of the 1964 rupture, we find no evidence for a prominent low-velocity layer above the slab Moho thick enough to be resolved by upgoing P-to-S conversions. These results support evidence from seismicity and geodetic strain suggesting that the 1964 rupture connected northern (Kenai) and southern (Kodiak) asperities with different plate interface properties.

Plain Language Summary

We use 398 portable seismometers that were deployed as part of the Alaska Amphibious Community Seismic Experiment to image the boundary between the subducting Pacific plate and the base of the North American plate. This seismic array with ~200 m spacing was deployed on Kodiak Island in 2019 within the southern rupture area of the 1964 Mw9.2 Great Alaska earthquake. We analyze conversions from compressional to shear waves from distant earthquakes to understand the conditions of the plate interface. Our results show a dipping velocity increase at ~30-40 km depth at the expected location of the Pacific slab crust-mantle boundary. In contrast to prior results from the northern 1964 rupture zone, we do not find a low-velocity layer atop the subducting plate. Our results indicate that the 1964 rupture connected segments of the Alaskan subduction zone with different plate interface properties.

1 Introduction

Understanding plate interface structure and subduction geometries can illuminate slip mechanisms, earthquake rupture behavior and shallow subduction zone processes. Because most global forearc regions are submerged, they are commonly studied via marine seismic methods, which, thus far, precludes dense-array natural source seismic imaging. Therefore, well-exposed forearcs such as Kodiak Island provide rare opportunities to study subduction zone and plate interface structure within the shallow forearc using a dense seismic array. Here, we use three-component node array data acquired in 2019 across northeastern Kodiak Island as part of the Alaska Amphibious Community Seismic Experiment (AACSE) to compute Ps teleseismic receiver functions (RFs) to better understand the nature of the plate interface in the rupture area of the 1964 Mw9.2 Great Alaska earthquake.

The Alaska-Aleutian subduction zone has hosted more M>8 earthquakes than any other system globally and offers opportunities to explore relationships between megathrust slip phenomena, seismicity, deformation and forearc structure. The Kodiak node array (Fig. 1) lies within the southern rupture area of the 1964 Mw9.2 Great Alaska earthquake, the second largest earthquake ever recorded (Kanamori, 1977, Fig. 1a). Coseismic slip and ground shaking from this event created damage across a 600-800 km section of the Alaskan margin and triggered local and far-field tsunami. Previous work investigating static deformation, seismic waves, and tsunami propagation revealed two major coseismic slip asperities: the Kenai asperity in the north and the Kodiak asperity in the south (Christensen & Beck, 1994; Ichinose et al., 2007; Johnson et al., 1996; Suito & Freymueller, 2009; Fig. 1a). Differences in rupture behavior, locking and recurrence interval between these two regions suggest major differences in subduction and interface properties within south-central Alaska.

2 Geologic Background and Previous Geophysical Studies of the 1964 Rupture Area

Kodiak Island (*Qikertaq in Alutiiq*) is part of an archipelago that represents an exposed section of the Mesozoic-Tertiary Alaska-Aleutian accretionary complex

uplifted either via duplex accretion and underplating (Sample & Fisher, 1986), out-of-sequence splay faulting (e.g., Rowe et al., 2009), or a combination of these processes. The surface exposures consist of Jurassic to Eocene formations bounded by NW-dipping and NE-striking thrusts (Wilson et al., 2015; Fig. 1b). The thrust-bounded units get progressively younger towards the southeast, approaching the current subduction trench offshore (Fig. 1b). Potentially active Quaternary fault systems include the Albatross Bank, Kodiak Shelf and Narrow Cape fault zones (Figs. 1b, 1c and 1d)). Paleocene granitic intrusions (~58-50 Ma) from ridge subduction (Ayuso et al., 2009; Farris et al., 2006; Fig. 1b) form the mountainous spine of the island interior. In the duplex accretion and underplating scenario for Kodiak Island formation and deformation, a stacked section of marine sediments builds up near the subduction decollement, forming a series of flat-ramp-flat geometries of imbricated material at depth within the overriding plate (Sample & Fisher, 1986). The build-up of the underthrust material causes the accretionary prism to grow vertically, with minimal fault penetration or deformation within the overlying sediments. In the splay fault model, the island was uplifted due to deformation on one or several seaward-vergent thrusts possibly rooted at the megathrust.

Prior to our study, the 2007-2008 Multidisciplinary Observations of Onshore Subduction (MOOS; J. Li et al., 2013; Fig. 1a) measured structure and seismicity beneath the Kenai Peninsula in the northern 1964 rupture zone. The MOOS experiment included 34 broadband seismometers deployed at 10-15 km station spacing. Major results include RF imaging showing a 3-5 km-thick low velocity zone (LVZ) sandwiched between the overriding North American plate and the subducting Yakutat microplate (Y. Kim et al., 2014). This low-velocity zone suggests the presence of subducting sediments and/or the presence of fluids within or below the plate interface. Imaging via autocorrelation of P-wave coda from local earthquakes replicates these results and further suggests that S-wave velocity within this zone decreases with depth (D. Kim et al., 2019).

A more recent study of the subducting crust beneath southcentral Alaska suggests that the LVZ extends far beyond the location of the MOOS array. In their scattered-wave imaging of the subduction zone beneath southcentral Alaska, Mann et al. (2022) analyzed seismic data recorded by 218 broadband seismometers across southcentral Alaska. Using data from the Wrangell Volcanism and Lithospheric Fate (WVLF; Fig. 1a) array, the Broadband Experiment Across the Alaska Range (BEAAR; Fig 1a) array, the Transportable Array (TA) and the MOOS array, they found that the LVZ covers > 450 km of the subducting Yakutat terrane (Mann et al., 2022). Our study tests whether these features extend southward, controlling structure beneath northeast Kodiak Island.

3 Data and Methods

3.1 The AACSE

The AACSE took place in 2018-2019 between Kodiak Island and Sanak Island (Abers et al., 2019; Barcheck et al., 2020; Fig. 1a). All experiment data is

publicly available and was open immediately upon completion of quality assurance, control and archiving. The AACSE included 75 broadband ocean-bottom seismometers (OBS), 30 broadband land seismometers, several dozen additional nearby permanent and EarthScope Transportable Array seismometers, complementary strong motion sensors and absolute- and differential-pressure gauges, and >3,000 km of active source wide-angle refraction profiles collected by the R/V *Marcus G Langseth* (Barcheck et al., 2020). The Kodiak node array was deployed in 2019 as a supplement to the larger AACSE. The array consisted of 398 Fairfield autonomous node sensors (from PASSCAL and University of Utah) with 3-component 5-Hz geophones deployed along a ~50 km road network centered on the city of Kodiak (Figs. 1b, 1c and 1d). Sensors were deployed at ~200-300 m station spacing over the course of 6 days (May 18-24) and recovered over 3 days (June 19-21). The full array was operational for 25 days (May 25 – June 18). All continuous waveform data from the node array are available in PH5 format via IRIS Data Services (network code 8J from 2019).

3.2 Receiver Function Processing

Previous work shows that the autonomous three-component 5-Hz geophones used in this study can yield high quality RFs comparable with co-located broadband seismometers (Ward et al., 2018; Ward & Lin, 2017). Like those earlier studies, our short deployment period limited the number of teleseismic events for RF calculation. Out of ~86 teleseismic events >Mw 5.0 occurring within the 30°- 90° search radius, we retained 7 events (Table S1; Fig. S1(a) and S1(b)) that met the selection criteria: (1) a magnitude >5.5, (2) a 30° – 90° epicentral distance from the center of the array, and (3) a signal-to-noise ratio (SNR)>3 and an identifiable incident P wave across the array (Figure S1(c)).

Prior to calculating RFs, we windowed the seismograms from 15 s before to 75 s after the theoretical P arrival. Next, we decimated the waveforms to 50 samples per second using an finite impulse response filter to prevent aliasing. We then removed the mean and the trend and applied a Hanning taper. Finally, we removed the instrument response from the nodal geophones (5 Hz corner frequency). We followed the above steps as outlined by Ward et al. (2018). We then filtered the resulting time series using a bandpass of 0.2 – 2.0 Hz. To groundtruth our waveform processing workflow, we retrieved waveforms for the selected 7 events recorded by AACSE broadband stations deployed within the node array footprint (Z. Li et al., 2020), performed the same preprocessing procedure, and compared the resultant broadband waveforms with the pre-processed nodal time series (Fig. S2).

After preprocessing, we culled additional noisy signals by applying a SNR-based noise reduction procedure which eliminated traces with SNR< 2.0 on the vertical component or SNR < 1.25 on the north component. Then we rotated from the station ZNE (vertical, north, east) coordinate system to the earthquake ZRT (vertical, radial, transverse) system. To compute the RFs for each event, we deconvolved the radial component seismograms with vertical component seismograms at each station using the time-domain iterative deconvolution method

(Ligorria & Ammon, 1999) with a Gaussian filter parameter of 2.5 (~1.2 Hz) and 5.0 (~2.4 Hz). All analysis was performed via Python using the open-source rf software package (Eulenfeld, 2020).

Before stacking the RFs, we applied a Ps phase moveout correction using the iasp91 (Kennett & Engdahl, 1991) model and calculated piercing points. We set the piercing point depth at 20 km based on estimates of slab depth (20 – 27 km) beneath the study area from the Slab2.0 model (Hayes et al., 2018), created equal profile boxes along the array (Fig. S3), and then stacked the receiver functions by common conversion points (Fig. 2). Both the stacked 1.2 and 2.4 Hz RFs were converted to depth (Fig. 2b and 2c) using the rf software and the iasp91 velocity model.

3.3 1-D Synthetic Modeling

To aid in our interpretation, we produced synthetic receiver functions (assuming a ray parameter of 0.05 s/km) that tested three simple velocity-density models of the structure below Kodiak Island. Our primary goal was to evaluate resolution of hypothetical structures near the top of the subducting oceanic crust. To better account for the RF variability across the profile, we selected groups of RFs from three different sections (6 km bins, centered at 10, 22 and 32 km distance along the profile) which showed good signal-to-noise ratios (Fig. 2c) and linearly stacked them. We then used the position of the slab Moho Ps arrival on the resultant stacked traces to help with the construction of the models (Figs. 3a-c).

Model 1 (Table 1; Fig. 3a) was based on the Kim et al. (2014) Kenai Peninsula model beneath the Kenai asperity. The model consists of a featureless upper crust, a 3 km-thick LVZ at the plate interface and an 8 km-thick oceanic crust. For model 2 (Table 1; Fig. 3b), we removed the 3-km-thick LVZ and calculated synthetics using just the featureless upper crust and the 8 km-thick oceanic crust. Model 3 (Table 1; Fig. 3c) is a simple two-layer model with an increase in velocity at the slab Moho depth.

4 Results

4.1 Receiver Function Imaging

Our final common conversion point stack produces a NW-SE-trending, approximately trench-perpendicular profile that samples a ~50 km segment of the Alaska subduction forearc up to 80 km deep (Fig. 2). Both the stacked 1.2 Hz (Fig. 2a) and the stacked 2.4 Hz images (Fig. 2c) show a coherent, SE to NW dipping positive conversion at ~ 30-40 km depth consistent with the expected slab Moho depth from previous studies. For reference, we plotted earthquakes from the AACSE catalog (Ruppert et al., 2021a; Ruppert et al., 2021b) beneath the study area (57.40-58.0 N, 152.083-152.75 W) which are within one standard deviation of the mean hypocentral depth of 24.96 km on our CCP images (black dots in Fig. 2b and 2d). We also plotted the top of the slab depth from Hayes et al. (2018) and inferred the slab Moho depth assuming an 8-km thick oceanic

crust (blue and red dashed lines in Fig. 2b and 2d). We do not observe a negative top-of-slab conversion above the positive slab Moho conversion.

We observe intermittent segments of shallow (above ~10 km depth) positive conversions across the length of the profile in our high frequency (2.4 Hz) stacked image (Fig. 2d). One such horizon at ~ 5 km depth extends from about ~8-12 km along the profile, and another beneath Kalsin Bay at ~7 km depth extends from 28-35 km along the profile. Since the depths of these early arrivals vary along the line, the arrival times of their multiples are also different. A mixture of these reverberations and other possible primary arrivals could explain the chaotic character of the traces between ~ 5 km and 35 km depths. Increasing the Gaussian value to 10 (~4.8 Hz) did not increase the quality of the final image (Fig. S4).

4.2 Synthetic Modeling Results

Since we were only modeling the features at slab depth and only considering the upgoing Ps conversion, we calculated correlation coefficients of the predicted and the observed waveforms from 2 s after P arrival to 10 seconds after P arrival. Model 1 (Fig. 3a) produced the worst fitting synthetics of all three models (average correlation coefficient of -0.06). Model 2 (Fig. 3b) which consisted of a featureless upper crust and an 8 km-thick oceanic crust is better fit compared to the first model (average correlation coefficient of 0.45). Model 3 (Fig. 3c), the simple two-layer model with an increase in velocity at the slab Moho depth is the best fitting model with an average correlation coefficient of 0.53. The results suggest that the Vp, Vs and density above the slab Moho must be similar to obtain optimal fit to the observed data. In other words, introducing additional features in the model above the Moho, even an oceanic crust, creates synthetics that poorly match the observational data.

5 Discussion

5.1 Absence of Oceanic Crust Arrival

In subduction zone environments, RFs are commonly used to investigate plate interface structure since the method exploits the conversion of incident P waves from a teleseismic event to S waves at significant seismic-velocity discontinuities. RFs have identified LVZs along the plate interfaces in subduction zones globally as negative amplitude pulses atop positive amplitude pulses at slab depth (Bostock, 2013; Audet & Kim, 2016). This dipole character has been observed in the Japan (Kawakatsu & Watada, 2007; Akuhara et al., 2017), Cascadia (Janiszewski & Abers, 2015; Ward et al., 2018), Costa Rica (Audet & Schwartz, 2013), Mariana (Tibi et al., 2008), Alaska (Ferris et al., 2003), and the central Mexico (Pérez-Campos et al., 2008; Y. Kim et al., 2012) subduction zones. Depending on how far down dip the study area is located, the negative pulse is typically interpreted as hydrated oceanic crust or mantle hydrated by fluid expelled from the subducting slab due to the low S-wave velocities observed, while the positive amplitude pulse is generally the slab Moho. In Cascadia, Janiszewski and Abers (2015) interpreted the LVZ as metamorphosed

sediments, while Bangs et al. (2009) interpreted the LVZ in Nankai as high porosity underthrust sediment. In the northern 1964 segment, Y. Kim et al. (2014) also observed this typical negative-to-positive character, attributing the negative arrivals to an LVZ of subducted marine sediments along the plate interface.

Neither our observed nor the preferred synthetic RFs (Figs 2 and 3) feature the negative-positive dipole character observed within the northern 1964 asperity, highlighting a major difference in RF character. The lack of major arrivals before the positive slab Moho suggests that beneath Kodiak, the seismic properties at the base of the upper plate and top of the subducting slab may be similar. Plate interface material is commonly inferred from trench sediment input to the subduction zone (Morgan, 2004; Underwood, 2007). At the trench near Kodiak, both pelagic sediments and sediment from the Surveyor Fan (von Huene et al., 2012; Reece et al., 2011; Fig. 1a) comprise the subduction input. We suggest that the subduction zone environment has altered the properties of any subducted sediment at the interface, thus suppressing contrast between the sediment and the surrounding rock. There is ample evidence from magnetotelluric (Heise et al., 2012), laboratory (Miller et al., 2021) and field studies of exhumed metasedimentary rocks from subduction zone forearcs (Rowe et al., 2009; Rowe et al., 2013) pointing to instances of hundreds of meters of metamorphosed sediments padding the plate interface. Therefore, the absence of a well-defined LVZ channel at the plate interface beneath our study area does not necessarily mean an absence of subducted sediment. The metasedimentary rocks on Kodiak Island are close enough in velocity (Miller et al., 2021) and density to the Pacific crust that there is no significant discontinuity at the interface to resolve with Ps RFs.

While the Ps RFs presented use relatively high frequencies for teleseismic imaging (1.2 – 2.5 Hz), there may be coherent structural layers that are too thin to be resolved. For example, using controlled source seismic reflection data, J. Li et al. (2015) estimated a thin 600-900 m low-velocity channel at ~8-10 km depth along the plate interface south of Kodiak Island inside the 1938 Mw 8.2 Semidi rupture zone. A synthetic test of 2.5 Hz Ps RFs showed that a 750 m thick LVZ would not be well resolved (Fig. S4(a)). We also tested using higher frequency observations, 4.8 Hz, but the signal-to-noise ratio of teleseismic sources decreases and the prominent velocity increase interpreted as the slab Moho is only resolved sporadically across the array (Fig. S4(b)). In areas where potential slab Moho arrivals are observed in the 4.8 Hz RF image, we still do not find evidence for an overlying LVZ (Fig. S4(b)). Thus, we cannot rule out a thin LVZ like that imaged at shallower depths in the Semidi rupture zone (J. Li et al., 2015), but we can be confident that a thicker LVZ (~3-5 km) like that imaged by Kim et al. (2014) in the Kenai asperity would be resolvable if it existed beneath our study area. Mann et al. (2022) used scattered P and S coda of teleseismic P waves to successfully image a continuous ~7-km thick low-velocity layer lining the top of the subducted Yakutat crust. While we see reverberations in sections of our profile (e.g., Fig. S5), their quality is too low to allow for interpretation. The

short deployment window (~25 days) and the limited backazimuth distribution of the events used in this study limits the usefulness of later arrivals.

5.2 Evidence of Rupture Across a Heterogeneous Plate Interface

The simple plate interface observed in our Kodiak study compared to the more complicated plate interface structure beneath the Kenai Peninsula supports other evidence that the 1964 earthquake ruptured across distinctive asperities. During the 1964 event, the northern Kenai asperity slipped an average of 18 m, while Kodiak slipped an average of ~10 m (Johnson et al., 1996). Major earthquakes in the Kenai area have a recurrence interval of 700-800 years (Wesson et al., 1999) and the plate interface is strongly locked (Zweck et al., 2002). In Kodiak, major earthquake recurrence interval is 60 years (Nishenko & Jacob, 1990) and, while the southern end of Kodiak interface appears strongly locked (S. Li & Freymueller, 2018), locking decreases to the north. Subduction geometry in the Kenai segment is controlled by subduction of the Yakutat microplate, a thick, buoyant oceanic plateau (Christeson et al., 2010) and a thick, subducting sediment package (Y. Kim et al., 2014; Worthington et al., 2012). The plate interface here dips shallowly at ~3-4 degrees. In Kodiak, the Pacific plate subducts beneath North America at ~8 degrees, and incoming plate structure includes ~2.5 km-thick sediments from the distal Surveyor Fan (Reece et al., 2011) and the Kodiak-Bowie seamount chain (Fig. 1a).

In their study of Kodiak region seismicity between 1964 and 2001, Doser et al. (2002) found that, while most earthquakes occur within the downgoing plate, several events beneath southern Kodiak Island have depths and thrust faulting mechanisms consistent with seismicity on the interface. Detailed seismicity studies on the Kenai Peninsula using the MOOS array show a well-defined seismic zone concentrated in the down-going plate, just below the plate boundary, that parallels the megathrust zone and is dominated by normal faulting mechanisms (J. Li et al., 2013). In contrast to observations in the Kodiak region, active thrusting and seismicity on the plate interface itself was absent (J. Li et al., 2013), possibly related to thick sediment subduction that forms a smooth interface between the North American and Yakutat plates. Shallow seismicity in the upper plate is spread out across the Kenai Peninsula without clear lineation and focal mechanisms are thrust or strike-slip.

Large megathrust earthquakes at other subduction zones, such as the 1700 M 9.0 Cascadia (Wang et al., 2013), 2011 M 9.0 Tohoku-Oki (Wei et al., 2012), 2004 M 9.2 Sumatra (Chlieh et al., 2007), and the 2011 M 8.8 in Chile (Lorito et al., 2011) events encompassed patches of slip rates different from the ambient slip rates within their rupture extents. The ubiquity of heterogeneous coseismic slip during large earthquakes further illustrates that the Great Alaska earthquake entraining multiple major segments during rupture is not unique to the Alaska subduction zone.

6 Conclusions

We analyzed teleseismic P waves from 398 autonomous three-component 5-Hz

nodal geophones on Kodiak Island as part of the Alaska Amphibious Community Seismic Experiment. We calculated RFs with a Gaussian value of 2.5 (~1.2 Hz) and a Gaussian value of 5.0 (~2.4 Hz). The lower frequency (1.2 Hz) RFs were comparable to RFs from near-collocated broadband seismometers, and the higher frequency (2.4 Hz) RFs image produced more details. In both low and high frequency images, there is a coherent, SE to NW dipping positive phase at the expected slab Moho depth but no observable negative arrival to indicate phase conversions at the oceanic crust. To help explain the observed RFs, we calculated synthetic RFs from 1-D models. These synthetic tests suggest that the overriding forearc material and Pacific oceanic crust have nearly identical seismic velocities and densities. We conclude that the 1964 Great Alaska Earthquake ruptured beyond the extent of the low-velocity shear zone observed in the Kenai asperity into a structural setting beneath Kodiak Island with little seismic contrast across the plate boundary interface.

Data and Resources:

The nodal seismic data used in this study are available from the IRIS DMC (dmc.iris.edu) under the network code 8J (doi: 10.7914/SN/8J_2019). The IRIS DMC is supported by the National Science Foundation under Cooperative Support Agreement EAR-1851048. We obtained digital elevation data for Figures 1a and 1c from the GEBCO Compilation Group (doi:10.5285/a29c5465-b138-234d-e053-6c86abc040b9, last accessed August 2021). Geologic map data for Figure 1b and 1c was obtained from the USGS Scientific Investigations map 3340 (https://pubs.er.usgs.gov/publication/sim3340, last accessed August 2021).

Acknowledgements:

We acknowledge that the Alaska Amphibious Community Seismic Experiment was conducted within the present, ancestral, and unceded lands and waters of the Alutiiq/Sugpiaq, Unangax, Aleut and Central Yup'ik peoples. Seismic stations on Kodiak Island (Qikertaq) were placed within lands of the Koniag Alaska Native Regional Corporation, specifically within the lands of Ahkiok, Anton Larsen Bay, Larsen Bay, Leisnoi, Old Harbor, and Ouzinkie Alaska Native Village Corporations and Sun'aq (Kodiak City). We are grateful to these communities and cultures for the opportunity to learn about their lands and waters.

The Alaska Amphibious Community Seismic Experiment (AACSE) was funded by the NSF award OCE-1654568 to Cornell University. Nodal geophones were provided by the Incorporated Research Institutions for Seismology-Portable Array Seismic Studies of the Continental Lithosphere (IRIS-PASSCAL) Instrument Center, which is supported by the National Science Foundation's Seismological Facilities for the Advancement of Geoscience (SAGE) Award under Cooperative Support Agreement EAR-1851048. Dr. Jamie Farrell (University of Utah) provided additional nodes and assisted with logistics. This research was partially supported by EAR-1950328. The authors would also like to ac-

knowledge Lucia Gonzales (University of Texas at El Paso), Dr. Jenny Nakai (USGS - Alaska Volcano Observatory), and Dr. Doug Wiens (Washington University in St. Louis), for their work on the node deployment. Dr. Aubreya Adams (Colgate University), Alyssa Fintel (Purdue University) and other summer undergraduate participants assisted with node retrieval and demobilization.

References

Abers, G. A., Adams, A. N., Haeussler, P. J., Roland, E., Shore, P. J., Schwartz, S. Y., Sheehan, A. F., Shillington, D. J., Webb, S., Wiens, D. A., and Worthington, L. L. (2019). AACSE: The Alaska amphibious community seismic experiment. *EOS Trans. AGU*, Online publ. 26 March 2019. https://eos.org/project-updates/examining-alaskas-earthquakes-on-land-and-sea.

Akuhara, T., Mochizuki, K., Kawakatsu, H., & Takeuchi, N. (2017). A fluid-rich layer along the Nankai trough megathrust fault off the Kii Peninsula inferred from receiver function inversion. *J Geophys Res B Solid Earth Planets*, *122*(8), 6524–6537. https://doi.org/10.1002/2017JB013965

Audet, P., & Kim, Y. (2016). Teleseismic constraints on the geological environments of deep episodic slow earthquakes in subduction zone forearcs: A review. *Tectonophysics*, *670*, 1-15. https://doi.org/10.1016/j.tecto.2016.01.005

Audet, P., & Schwartz, S. Y. (2013). Hydrologic control of forearc strength and seismicity in the Costa Rican subduction zone. *Nat Geosci*, *6(10)*, 852-855. https://doi.org/10.1038/ngeo1927

Ayuso, R. A., Haeussler, P. J., Bradley, D. C., Farris, D. W., Foley, N. K., & Wandless, G. A. (2009). The role of ridge subduction in determining the geochemistry and Nd–Sr–Pb isotopic evolution of the Kodiak batholith in southern Alaska. *Tectonophysics*, *464*(1–4), 137–163. https://doi.org/10.1016/j.tecto.2008.09.029

Bangs, N. L. B., Moore, G. F., Gulick, S. P. S., Pangborn, E. M., Tobin, H. J., Kuramoto, S., & Taira, A. (2009). Broad, weak regions of the Nankai Megathrust and implications for shallow coseismic slip. *Earth Planet Sci Lett*, *284*(1–2), 44–49. https://doi.org/10.1016/j.epsl.2009.04.026

Barcheck, G., Abers, G. A., Adams, A. N., Bécel, A., Collins, J., Gaherty, J. B., Haeussler, P.J., Li, Z., Moore, G., Onyango, E. A., Roland, E., Sampson, D. E., Schwartz, S. Y., Sheehan, A. F., Shillington, D. J., Shore, P. J., Webb, S., Wiens, D. A., & Worthington, L. L. (2020). The Alaska Amphibious Community Seismic Experiment. *Seismol Res Lett*, *91*(6), 3054–3063. https://doi.org/10.1785/0220200189

Bostock, M. G. (2013). The Moho in subduction zones. *Tectonophysics*, *609*, 547–557. https://doi.org/10.1016/j.tecto.2012.07.007

Chlieh, M., Avouac, J. P., Hjorleifsdottir, V., Song, T. R. A., Ji, C., Sieh, K., Sladen, A., Hebert, H., Prawirodirdjo, L., Bock, L., & Galetzka,

J. (2007). Coseismic Slip and Afterslip of the Great Mw 9.15 Sumatra-Andaman Earthquake of 2004. *Bull Seismol Soc Am*, *97*(1A), S152–S173. https://doi.org/10.1785/0120050631

Christensen, D. H., & Beck, S. L. (1994). The rupture process and tectonic implications of the great 1964 Prince William Sound earthquake. *Pure Appl Geophys*, *142*(1), 29–53.

Christeson, G. L., Gulick, S. P. S., van Avendonk, H. J. A., Worthington, L. L., Reece, R. S., & Pavlis, T. L. (2010). The Yakutat terrane: Dramatic change in crustal thickness across the Transition fault, Alaska. *Geology*, *38*(10), 895–898. https://doi.org/10.1130/G31170.1

Doser, D. I., Brown, W. A., & Velasquez, M. (2002). Seismicity of the Kodiak Island Region (1964-2001) and Its Relation to the 1964 Great Alaska Earthquake. *Bull Seismol Soc Am*, *92*(8), 3269–3292. https://doi.org/10.1785/0120010280

Eulenfeld, T. (2020). rf: Receiver function calculation in seismology. *Journal of Open Source Software*, *5*(48), 1808. https://doi.org/10.21105/joss.01808

Farris, D. W., Haeussler, P., Friedman, R., Paterson, S. R., Saltus, R. W., & Ayuso, R. (2006). Emplacement of the Kodiak batholith and slab-window migration. *Geol Soc Am Bull*, *118*(11–12), 1360–1376. https://doi.org/10.1130/B25718.1

Ferris, A., Abers, G. A., Christensen, D. H., & Veenstra, E. (2003). High resolution image of the subducted Pacific (?) plate beneath central Alaska, 50–150 km depth. *Earth Planet Science Lett*, *214*(3–4), 575–588. https://doi.org/10.1016/S0012-821X(03)00403-5

Hayes, G. P., Moore, G. L., Portner, D. E., Hearne, M., Flamme, H., Furtney, M., & Smoczyk, G. M. (2018). Slab2, a comprehensive subduction zone geometry model. *Science*, *362*(6410), 58–61. https://doi.org/10.1126/science.aat4723

Heise, W., Caldwell, T. G., Hill, G. J., Bennie, S. L., Wallin, E., & Bertrand, E. A. (2012). Magnetotelluric imaging of fluid processes at the subduction interface of the Hikurangi margin, New Zealand. *Geophys Res Lett*, *39*(4). https://doi.org/10.1029/2011GL050150

von Huene, R., Miller, J. J., & Weinrebe, W. (2012). Subducting plate geology in three great earthquake ruptures of the western Alaska margin, Kodiak to Unimak. *Geosphere*, *8*(3), 628–644. https://doi.org/10.1130/GES00715.1

Ichinose, G., Somerville, P., Thio, H. K., Graves, R., & O'Connell, D. (2007). Rupture process of the 1964 Prince William Sound, Alaska, earthquake from the combined inversion of seismic, tsunami, and geodetic data. *J Geophys Res*, *112*(B7), B07306. https://doi.org/10.1029/2006JB004728

Janiszewski, H. A., & Abers, G. A. (2015). Imaging the Plate Interface in the Cascadia Seismogenic Zone: New Constraints from Offshore Receiver Functions. *Seismol Res Lett*, *86*(5), 1261–1269. https://doi.org/10.1785/0220150104

Johnson, J. M., Satake, K., Holdahl, S. R., & Sauber, J. (1996). The 1964 Prince William Sound earthquake: Joint inversion of tsunami and geodetic data. *J Geophys Res B Solid Earth Planets*, *101*(B1), 523–532. https://doi.org/10.1029/95JB02806

Kanamori, H. (1977). The energy release in great earthquakes. *J Geophys Res*, *82*(20), 2981–2987. https://doi.org/10.1029/JB082i020p02981

Kawakatsu, H., & Watada, S. (2007). Seismic Evidence for Deep-Water Transportation in the Mantle. *Science*, *316*(5830), 1468–1471. https://doi.org/10.1126/science.1140855

Kennett, B. L. N., & Engdahl, E. R. (1991). Traveltimes for global earthquake location and phase identification. *Geophys J Int*, *105*(2), 429–465. https://doi.org/10.1111/j.1365-246X.1991.tb06724.x

Kim, D., Keranen, K. M., Abers, G. A., & Brown, L. D. (2019). Enhanced Resolution of the Subducting Plate Interface in Central Alaska From Autocorrelation of Local Earthquake Coda. *J Geophys Res B Solid Earth Planets*, *124*(2), 1583–1600. https://doi.org/10.1029/2018JB016167

Kim, Y., Miller, M. S., Pearce, F., & Clayton, R. W. (2012). Seismic imaging of the Cocos plate subduction zone system in central Mexico. *G-cubed*, *13*(7). https://doi.org/10.1029/2012GC004033

Kim, Y., Abers, G. A., Li, J., Christensen, D., Calkins, J., & Rondenay, S. (2014). Alaska Megathrust 2: Imaging the megathrust zone and Yakutat/Pacific plate interface in the Alaska subduction zone. *J Geophys Res B Solid Earth Planets*, *119*(3), 1924–1941. https://doi.org/10.1002/2013JB010581

Li, J., Abers, G. A., Kim, Y., & Christensen, D. (2013). Alaska megathrust 1: Seismicity 43 years after the great 1964 Alaska megathrust earthquake. *J Geophys Res B Solid Earth Planets*, *118*(9), 4861–4871. https://doi.org/10.1002/jgrb.50358

Li, J., Shillington, D. J., Bécel, A., Nedimović, M. R., Webb, S. C., Saffer, D. M., Keranen, K. M., & Kuehn, H. (2015). Downdip variations in seismic reflection character: Implications for fault structure and seismogenic behavior in the Alaska subduction zone. *J Geophys Res B Solid Earth Planets*, *120*(11), 7883–7904. https://doi.org/10.1002/2015JB012338

Li, S., & Freymueller, J. T. (2018). Spatial Variation of Slip Behavior Beneath the Alaska Peninsula Along Alaska-Aleutian Subduction Zone. *Geophys Res Lett*, *45*(8), 3453–3460. https://doi.org/10.1002/2017GL076761

Li, Z., Wiens, D., & Shen, W. (2020). Crust and Uppermost Mantle Structure of the Alaska Subduction Zone from Joint Inversion of Rayleigh Wave Dispersion and Receiver Functions. *The 2020 AGU Fall Meeting,* Online, 1-17 December, Abstract T055-04.

Ligorria, J. P., & Ammon, C. J. (1999). Iterative Deconvolution and Receiver-Function Estimation. *Bull Seismol Soc Am*, *89*(5), 1395–1400.

Lorito, S., Romano, F., Atzori, S., Tong, X., Avallone, A., McCloskey, J., Cocco, M., Boschi, E., & Piatanesi, A. (2011). Limited overlap between the seismic gap and coseismic slip of the great 2010 Chile earthquake. *Nat Geosci*, *4*(3), 173–177. https://doi.org/10.1038/ngeo1073

Mann, M. E., Abers, G. A., Daly, K. A., & Christensen, D. H. (2022). Subduction of an Oceanic Plateau Across Southcentral Alaska: Scattered-Wave Imaging. *J Geophysl Res B Solid Earth Planets*, *127*(1), e2021JB022697. https://doi.org/10.1029/2021JB022697

Miller, P. K., Saffer, D. M., Abers, G. A., Shillington, D. J., Bécel, A., Li, J., & Bate, C. (2021). P- and S-Wave Velocities of Exhumed Metasediments From the Alaskan Subduction Zone: Implications for the In Situ Conditions Along the Megathrust. *Geophys Res Lett*, *48*(20), e2021GL094511. https://doi.org/10.1029/2021GL094511

Morgan, J. K. (2004). Consolidation state and strength of underthrust sediments and evolution of the décollement at the Nankai accretionary margin: Results of uniaxial reconsolidation experiments. *J Geophys Res*, *109*(B3), B03102. https://doi.org/10.1029/2002JB002335

Nishenko, S. P., & Jacob, K. H. (1990). Seismic potential of the Queen Charlotte-Alaska-Aleutian Seismic Zone. *J Geophys Res*, *95*(B3), 2511. https://doi.org/10.1029/JB095iB03p02511

Pérez-Campos, X., Kim, Y., Husker, A., Davis, P. M., Clayton, R. W., Iglesias, A., Pacheco, J. F., Singh, S. K., Manea, V. C., & Gurnis, M. (2008). Horizontal subduction and truncation of the Cocos Plate beneath central Mexico. *Geophys Res Lett*, *35*(18), L18303. https://doi.org/10.1029/2008GL035127

Reece, R. S., Gulick, S. P. S., Horton, B. K., Christeson, G. L., & Worthington, L. L. (2011). Tectonic and climatic influence on the evolution of the Surveyor Fan and Channel system, Gulf of Alaska. *Geosphere*, *7*(4), 830–844. https://doi.org/10.1130/GES00654.1

Rowe, Christen D, Meneghini, F., & Moore, J. C. (2009). Fluid-rich damage zone of an ancient out-of-sequence thrust, Kodiak Islands, Alaska. *Tectonics*, *28*(1). https://doi.org/10.1029/2007TC002126

Rowe, Christie D, Moore, J. C., & Remitti, F. (2013). The thickness of subduction plate boundary faults from the seafloor into the seismogenic zone. *Geology*, *41*(9), 991–994. https://doi.org/10.1130/G34556.1

Ruppert, N. A., Barcheck, G., & Abers, G. A. (2021a). AACSE earthquake catalog: May-December, 2018. http://hdl.handle.net/11122/11418

Ruppert, N. A., Barcheck, G., & Abers, G. A. (2021b). AACSE earthquake catalog: January-August, 2019. http://hdl.handle.net/11122/11967

Sample, J. C., & Fisher, D. M. (1986). Duplex accretion and underplating in an ancient accretionary complex, Kodiak Islands, Alaska. *Geology*, *14*(2), 160–163. https://doi.org/10.1130/0091-7613(1986)14<160:DAAUIA>2.0.CO;2

Suito, H., & Freymueller, J. T. (2009). A viscoelastic and afterslip postseismic deformation model for the 1964 Alaska earthquake. *J Geophys Res B Solid Earth Planets*, *114*(B11). https://doi.org/10.1029/2008JB005954

Tibi, R., Wiens, D. A., & Yuan, X. (2008). Seismic evidence for widespread serpentinized forearc mantle along the Mariana convergence margin. *Geophys Res Lett*, *35*(13), L13303. https://doi.org/10.1029/2008GL034163

Underwood, M. B. (2007). Sediment Inputs to Subduction Zones: Why lithostratigraphy and clay mineralogy matter. In *The Seismogenic Zone of Subduction Thrust Faults* (pp. 42–85). Columbia University Press. https://doi.org/10.7312/dixo13866-003

Wang, P. L., Engelhart, S. E., Wang, K., Hawkes, A. D., Horton, B. P., Nelson, A. R., & Witter, R. C. (2013). Heterogeneous rupture in the great Cascadia earthquake of 1700 inferred from coastal subsidence estimates. *J Geophys Res B Solid Earth Planets*, *118*(5), 2460–2473. https://doi.org/10.1002/jgrb.50101

Ward, K. M., & Lin, F. (2017). On the Viability of Using Autonomous Three-Component Nodal Geophones to Calculate Teleseismic Ps Receiver Functions with an Application to Old Faithful, Yellowstone. *Seismol Res Lett*, *88*(5), 1268–1278. https://doi.org/10.1785/0220170051

Ward, K. M., Lin, F., & Schmandt, B. (2018). High-Resolution Receiver Function Imaging Across the Cascadia Subduction Zone Using a Dense Nodal Array. *Geophys Res Lett*, *45*(22), 12,218-12,225. https://doi.org/10.1029/2018GL079903

Wei, S., Graves, R., Helmberger, D., Avouac, J. P., & Jiang, J. (2012). Sources of shaking and flooding during the Tohoku-Oki earthquake: A mixture of rupture styles. *Earth Planet Sci Lett*, *333–334*, 91–100. https://doi.org/10.1016/j.epsl.2012.04.006

Wesson, R. L., Frankel, A. D., Mueller, C. S., & Harmsen, S. C. (1999). Probabilistic seismic hazard maps of Alaska. *US Geol. Surv. Open-File Rept. 99-36*. https://doi.org/10.3133/ofr9936

Wilson, F. H., Hults, C. P., Mull, C. G., & Karl, S. M. (2015). *Geologic map of Alaska. Scientific Investigations Map. US Geol. Surv. Open-File Rept. 3340*. https://doi.org/10.3133/sim3340

Worthington, L. L., Van Avendonk, H. J. A., Gulick, S. P. S., Christeson, G. L., & Pavlis, T. L. (2012). Crustal structure of the Yakutat terrane and the evolution of subduction and collision in southern Alaska. *J Geophys Res B Solid Earth Planets*, *117*(B1). https://doi.org/10.1029/2011JB008493

Zweck, C., Freymueller, J. T., & Cohen, S. C. (2002). Three-dimensional

elastic dislocation modeling of the postseismic response to the 1964 Alaska earthquake. *J Geophys Res B Solid Earth Planets*, *107*(B4), ECV-1. https://doi.org/10.1029/2001JB000409

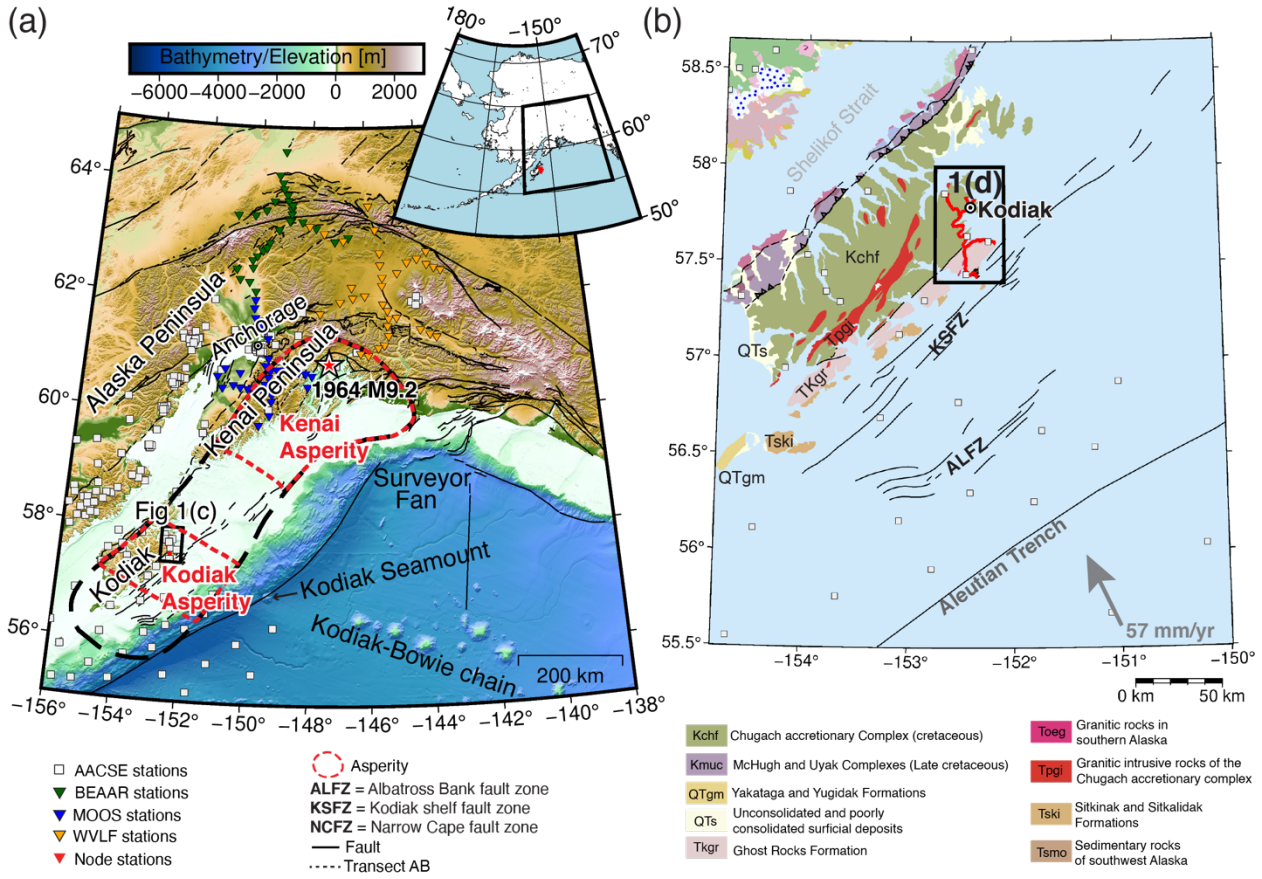
(a)
Bathymetry/Elevation [m]
−6000 −4000 −2000 0 2000
Alaska Peninsula
Anchorage
Kenai Peninsula
1964 M9.2
Kenai Asperity
Surveyor Fan
Fig. 1(c)
Kodiak
Kodiak Asperity
Kodiak Seamount
Kodiak-Bowie chain
200 km
AACSE stations
BEAAR stations
MOOS stations
WVLF stations
Node stations
Asperity
ALFZ = Albatross Bank fault zone
KSFZ = Kodiak shelf fault zone
NCFZ = Narrow Cape fault zone
Fault
Transect AB
(b)
Shelikof Strait
1(d)
Kodiak
Kchf
QTs
Tpgi
Tkgr
Tski
QTgm
KSFZ
ALFZ
Aleutian Trench
57 mm/yr
0 km 50 km
Kchf Chugach accretionary Complex (cretaceous)
Kmuc McHugh and Uyak Complexes (Late cretaceous)
QTgm Yakataga and Yugidak Formations
QTs Unconsolidated and poorly consolidated surficial deposits
Tkgr Ghost Rocks Formation
Toeg Granitic rocks in southern Alaska
Tpgi Granitic intrusive rocks of the Chugach accretionary complex
Tski Sitkinak and Sitkalidak Formations
Tsmo Sedimentary rocks of southwest Alaska
(c)
A
KD02
Kodiak
Womens Bay
Middle Bay
KD01
Kalsin Bay
KS03
NCFZ
KD00
B
0 km 10 km
(d)
Tpgi
Kchf
Tkgr
Tsmo
Toeg

Figure 1. Maps of southern Alaska, Kodiak Island and the study area. **(a)** Topography and faults of the Kodiak Islands region. MOOS array (blue triangles), BEAAR array (green triangles), WVLF array (Orange triangles). **(b)** Geology map of the Kodiak Islands region. Refer to Wilson et al., (2015) for geologic unit explanation. **(c)** Shaded topographic map of the study area. **(d)** Geological map of the study area. Refer to Wilson et al., (2015) for geologic unit explanation.

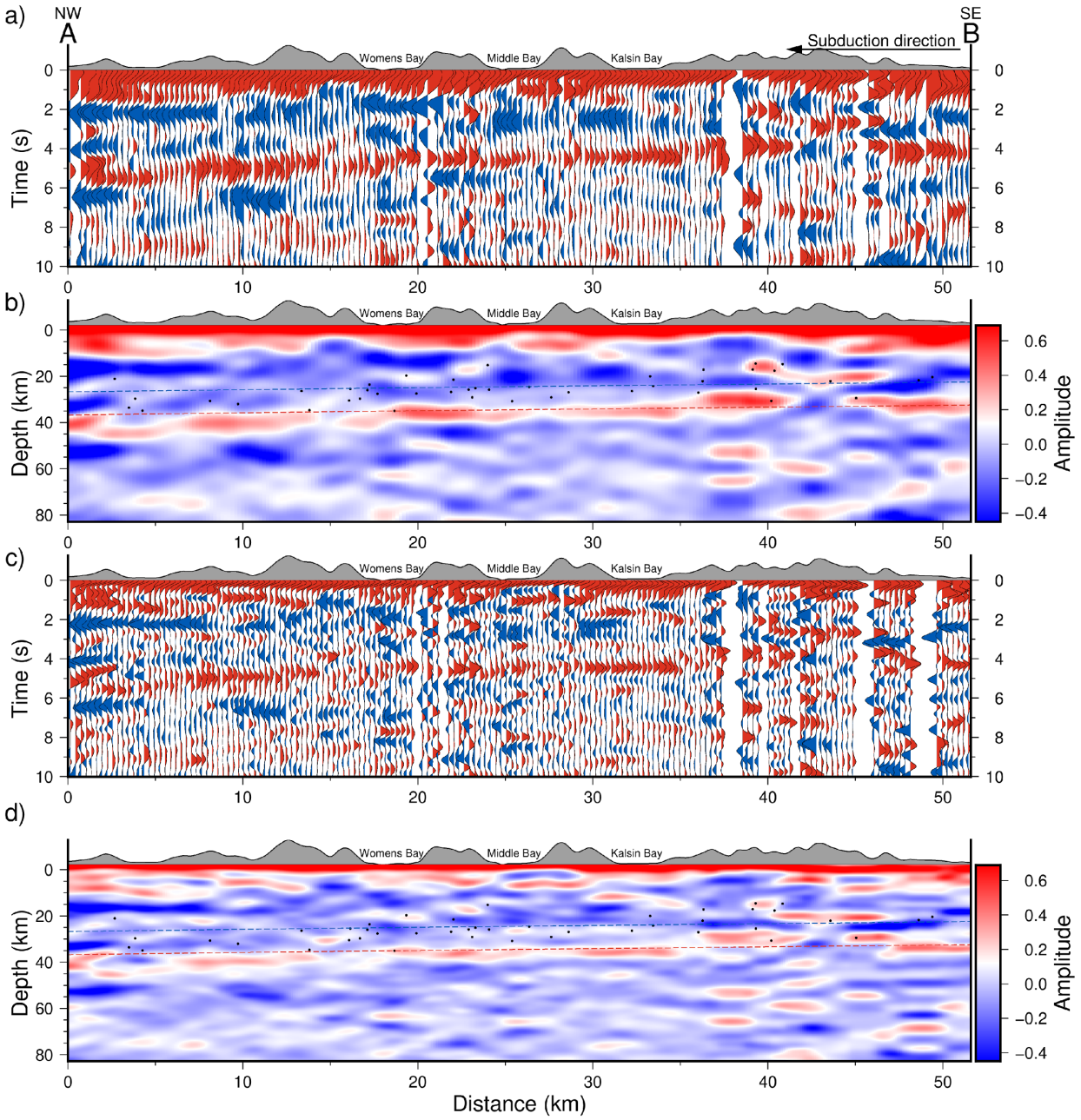

Figure 2. **(a)** Stacked radial receiver functions with a Gaussian value of 2.5 (~ 1.2 Hz). **(b)** ~1.2 Hz CCP image for transect A-B. Note the clear lack of a low velocity channel at the plate interface (Red = Positive, Blue = Negative). For reference, earthquakes from the AACSE catalog (black dots) and the slab depth

of Hayes et al. (2018) are plotted as blue dashes and inferred Moho surface (red dashes) assuming an 8-km thick oceanic crust. **(c)** Stacked radial receiver functions with a Gaussian value of 5.0 (~2.4 Hz). Stack1, Stack2 and Stack3 show the locations of the receiver functions stacked and plotted in Figure 4 to compare with synthetics. **(d)** ~2.4 Hz CCP image for transect A-B. Note the clear lack of a low velocity channel at the plate interface. For reference, earthquakes from the AACSE catalog (black dots) and the slab depth of Hayes et al. (2018) are plotted as blue dashes and inferred Moho surface (red dashes) assuming an 8-km thick oceanic crust. Vertical exaggeration = 0.135.

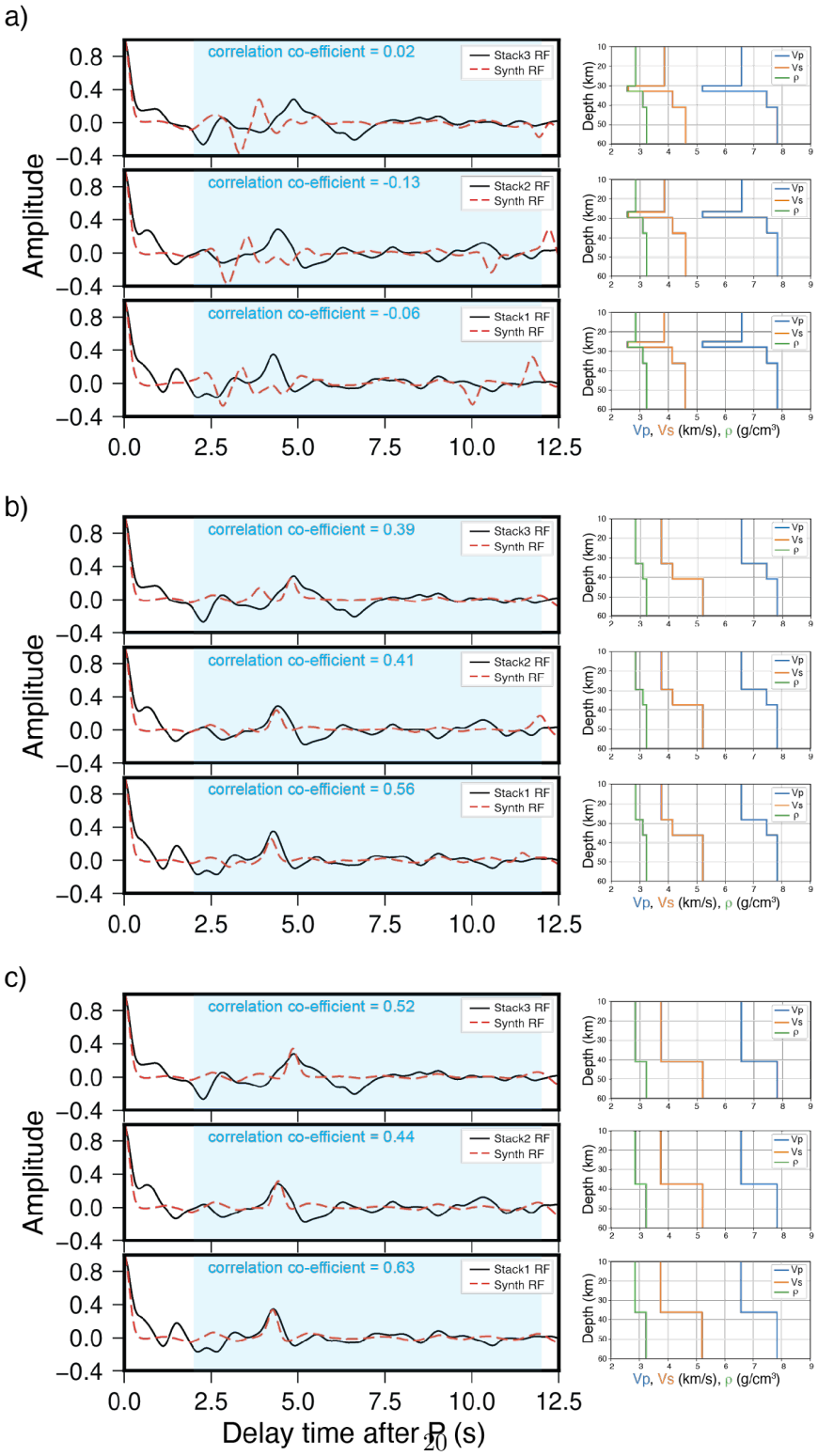
a)
b)
c)
correlation co-efficient = 0.02
correlation co-efficient = -0.13
correlation co-efficient = -0.06
correlation co-efficient = 0.39
correlation co-efficient = 0.41
correlation co-efficient = 0.56
correlation co-efficient = 0.52
correlation co-efficient = 0.44
correlation co-efficient = 0.63
Stack3 RF
Stack2 RF
Stack1 RF
Synth RF
Amplitude
Delay time after P (s)
Depth (km)
Vp
Vs
ρ
Vp, Vs (km/s), ρ (g/cm³)

Figure 3. Synthetic modeling results overlaid on stacked field RFs at different points along the profile (left column). The right column contains the velocity models used to calculate the synthetic RFs on the left. **(a)** Model 1. Synthetic RF (red dashed lines) overlaid on stacked field RF stack centered at 10 km (top panel). Synthetic RF overlaid on field RF stack centered at 22 km (middle panel). Synthetic RF overlaid on field RF stack centered at 32 km (bottom panel). **(b)** Model 2. Synthetic RF (red dashed lines) overlaid on stacked field RF stack centered at 10 km (top panel). Synthetic RF overlaid on field RF stack centered at 22 km (middle panel). Synthetic RF overlaid on field RF stack centered at 32 km (bottom panel). **(c)** Model 3 is the best-fitting model. Synthetic RF (red dashed lines) overlaid on stacked field RF stack centered at 10 km (top panel). Synthetic RF overlaid on field RF stack centered at 22 km (middle panel). Synthetic RF overlaid on field RF stack centered at 32 km (bottom panel).

Table 1. One-Dimensional model parameters

Model1	V_P **(km/s)**	V_S **(km/s)**	V_P/V_S	**Density (g/cm3)**
Layer1	6.57	3.86	1.7	2.85
Layer2	5.20	2.60	2.0	2.57
Layer3	7.45	4.14	1.8	3.11
Layer4	7.83	4.61	1.7	3.23
Model2	V_P **(km/s)**	V_S **(km/s)**	V_P/V_S	**Density (g/cm3)**
Layer1	6.57	3.75	1.75	2.85
Layer2	7.45	4.14	1.8	3.11
Layer3	7.83	5.22	1.50	3.23
Model3	V_P **(km/s)**	V_S **(km/s)**	V_P/V_S	**Density (g/cm3)**
Layer1	6.57	3.75	1.75	2.85
Layer2	7.83	5.22	1.50	3.23